Hemodynamics in the mouse aortic arch as assessed by MRI, ultrasound, and numerical modeling

Akiva Feintuch, Permyos Ruengsakulrach, Amy Lin, Ji Zhang, Yu-Qing Zhou, Jonathon Bishop, Lorinda Davidson, David Courtman, F. Stuart Foster, David A. Steinman, R. Mark Henkelman and C. Ross Ethier

Am J Physiol Heart Circ Physiol 292:884-892, 2007. First published Sep 29, 2006;
doi:10.1152/ajpheart.00796.2006

Am J Physiol Heart Circ Physiol 292: H884–H892, 2007.
First published September 29, 2006; doi:10.1152/ajpheart.00796.2006.

Hemodynamics in the mouse aortic arch as assessed by MRI, ultrasound, and numerical modeling

Akiva Feintuch,[1] Permyos Ruengsakulrach,[3] Amy Lin,[4] Ji Zhang,[4] Yu-Qing Zhou,[1] Jonathon Bishop,[1] Lorinda Davidson,[1] David Courtman,[5] F. Stuart Foster,[6] David A. Steinman,[4,7] R. Mark Henkelman,[1,2] and C. Ross Ethier[4,7]

[1]*Mouse Imaging Centre, Hospital for Sick Children, Toronto;* [2]*Department of Medical Biophysics, University of Toronto;* [3]*Department of Mathematics, Mahidol University, Bangkok, Thailand;* [4]*Department of Mechanical and Industrial Engineering, University of Toronto;* [5]*St. Michael's Hospital, Toronto;* [6]*Sunnybrook Health Sciences Centre, Toronto; and* [7]*Institute of Biomaterials and Biomedical Engineering, University of Toronto, Toronto, Ontario, Canada*

Submitted 25 July 2006; accepted in final form 20 September 2006

Feintuch A, Ruengsakulrach P, Lin A, Zhang J, Zhou YQ, Bishop J, Davidson L, Courtman D, Foster FS, Steinman DA, Henkelman RM, Ethier CR. Hemodynamics in the mouse aortic arch as assessed by MRI, ultrasound, and numerical modeling. *Am J Physiol Heart Circ Physiol* 292: H884–H892, 2007. First published September 29, 2006; doi:10.1152/ajpheart.00796.2006.—Mice are widely used to study arterial disease in humans, and the pathogenesis of arterial diseases is known to be strongly influenced by hemodynamic factors. It is, therefore, of interest to characterize the hemodynamic environment in the mouse arterial tree. Previous measurements have suggested that many relevant hemodynamic variables are similar between the mouse and the human. Here we use a combination of Doppler ultrasound and MRI measurements, coupled with numerical modeling techniques, to characterize the hemodynamic environment in the mouse aortic arch at high spatial resolution. We find that the hemodynamically induced stresses on arterial endothelial cells are much larger in magnitude and more spatially uniform in the mouse than in the human, an effect that can be explained by fluid mechanical scaling principles. This surprising finding seems to be at variance with currently accepted models of the role of hemodynamics in atherogenesis and the known distribution of atheromatous lesions in mice.

atherogenesis; magnetic resonance imaging; finite element modeling; shear stress

MICE ARE NOW WIDELY USED as model organisms to study human disease, including atherosclerosis. Several mouse models of atherogenesis have been developed (for review see Refs. 2, 9, 29, and 35), many of which have examined disease development in the aorta because it is the largest and hence one of the most experimentally accessible arteries. Here we focus on the ascending aorta, the aortic arch, and the proximal portion of the descending aorta, where the distribution of atherosclerotic lesions and the expression patterns of proatherogenic factors show significant spatial heterogeneity (14, 26, 27, 32). More specifically, in murine models of atherogenesis, there is a propensity for lesions to develop at the aortic root, near the ostia of the three major branches in the arch, and on the inner radius (lesser curvature) as compared with the outer radius (greater curvature).

Studies in humans and large animal models (rabbits and pigs) have produced a significant body of evidence suggesting that spatial heterogeneity in atherosclerotic lesion development is, in large part, dependent on hemodynamic factors (8, 23, 43), the best studied of which is wall shear stress (3). It is generally believed that similar hemodynamic factors influence the distribution of atherosclerotic lesions in the mouse, although the hemodynamic environment in the mouse has not been well characterized. Hemodynamic variables that have been measured in the mouse include heart rate, cardiac output waveform, blood pressure, and aortic blood velocity (see, e.g., Refs. 10, 16, 17, and 42). On the basis of the similarity in anatomy, blood flow velocity, cardiac output waveform shape, and blood pressure, it has generally been assumed that the detailed hemodynamic patterns in the mouse aorta are substantially similar to those in humans and other larger animals.

Our goal was to characterize the hemodynamic environment in the aortic arch region of the mouse. We present evidence showing that blood flow patterns in the mouse aorta differ in important ways from those in the human aorta, a fact that has important implications for how we view the role of biomechanical factors in atherogenesis in the mouse.

MATERIALS AND METHODS

We studied hemodynamics in the mouse aorta using a combination of experimental measurements from imaging and numerical modeling. Numerical modeling, when informed by suitable experimental data, allows the characterization of hemodynamic parameters at experimentally inaccessible length scales. For experimental studies, all animal utilization protocols were approved by the Animal Care committees of the relevant hospitals (Hospital for Sick Children, Sunnybrook Health Sciences Centre, and St. Michael's Hospital), all of which were subject to the Canadian Council on Animal Care regulations.

Ultrasound imaging. Eight inbred C57BL/6 adult mice were studied (4 males and 4 females; 20–25 g body wt). Mice were anesthetized with ~1.5% isoflurane through a face mask and laid on a platform in the supine position with all legs taped to ECG electrodes for heart rate monitoring. Body temperature was monitored via a rectal thermometer (Indus Instruments, Houston, TX) and maintained at 36–38°C using a heating pad and lamp. All hair was removed from the chest using a chemical hair remover (Nair, Carter-Horner, Mississauga, ON, Canada). To provide a coupling medium for the transducer, a prewarmed ultrasound gel (Aquasonic 100; Parker, Orange, NJ) was spread over the chest wall.

Imaging using an ultrasound biomicroscope (Vevo 770, VisualSonics, Toronto, ON, Canada) commenced after waiting ~1–2 min for the mouse to stabilize (44). The single crystal mechanical transducer had

Address for reprint requests and other correspondence: C. R. Ethier, Institute of Biomaterials and Biomedical Engineering, Univ. of Toronto, 164 College St., Toronto, ON M5S 3G9 Canada (e-mail: ethier@mie.utoronto.ca).

The costs of publication of this article were defrayed in part by the payment of page charges. The article must therefore be hereby marked "*advertisement*" in accordance with 18 U.S.C. Section 1734 solely to indicate this fact.

a central frequency of 30 MHz and a focal length of 12.7 mm. The maximum field of view for 2D imaging was 20 mm × 20 mm with spatial resolution of ~100 μm (lateral) by ~65 μm (axial) in the focal zone. The repetition rate for M-mode recording was 1,000 Hz. In Doppler mode, the maximum pulse repetition frequency was 96 kHz, corresponding to a maximum unaliased velocity of 120 cm/s (with Doppler intercept angle being zero). This range of velocity measurement can be doubled by baseline shifting.

Blood flow velocity was measured at the middle level of the ascending aorta, proximal parts of the innominate artery, left common carotid artery, and left subclavian artery. Because of the nonuniform flow velocity distribution at those locations, a large Doppler sample volume was used, which covered the vessel lumens for the three major branch vessels and most of the vessel lumen for the ascending aorta (Fig. 1). Doppler velocity measurement was made with the smallest possible angle of incidence between the Doppler beam and the assumed blood flow direction in the targeted vessel. For diameter measurement at locations where the flow velocity was measured, M-mode recording was made in the section with largest lumen dimension and with the targeted vessels perpendicular to the ultrasound beam. The complete examination for each mouse lasted ~30–45 min.

Doppler spectra and M-mode recordings were quantified according to the standards set for humans, including correction for Doppler angle (36, 38). From Doppler spectra, peak flow velocity and time-velocity integral (TVI), based on automatic mean velocity tracing, were extracted and averaged for three consecutive cardiac cycles (Fig. 1). From the M-mode recording, the diameters of the vessel at the beginning of the ejection phase and at peak systole were measured for three cardiac cycles and averaged. These average diameters were then averaged together to give an overall average vessel diameter, *D*. The total blood volume passing the measure-

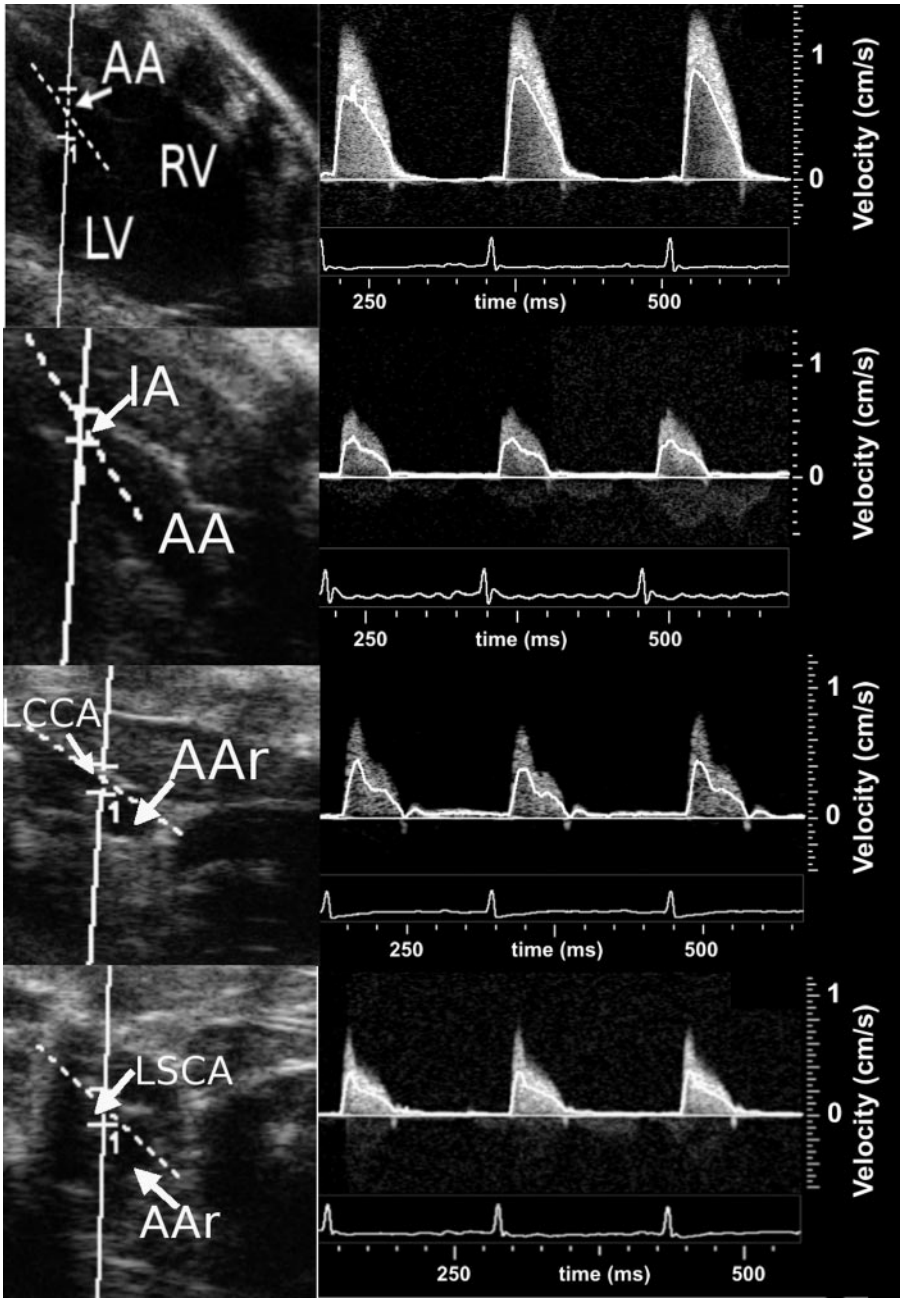

Fig. 1. High-resolution ultrasound imaging of blood flow patterns in the mouse aortic arch (AAr) and its major branches. *Left*: anatomical B-mode images with beam direction (solid line) and operator-defined vessel axis (dashed line) superimposed. *Right*: Doppler velocity spectra, with the mean velocity superimposed as a bright line, for the ascending aorta (AA), innominate artery (IA), left common carotid artery (LCCA), and left subclavian artery (LSCA), reading from *top* to *bottom*. RV, right ventricle; LV, left ventricle.

ment location per cardiac cycle flow at each location was calculated as $V = TVI\ \pi\ D^2/4$ (Fig. 1).

MRI. Blood flow patterns were measured in five inbred C57BL/6 mice (3 males and 2 females; 20–25 g body mass). The mice were anesthetized for the scan duration with a mixture of 1.6% isoflurane gas and oxygen. They were loaded on a custom-built sled (4) with a built-in physiological monitoring apparatus. ECG electrodes were fastened to the shaved chest with conductive hydrogel, while respiration was recorded with a pneumatic pillow. A commercial monitoring system (Small Animal Instruments, Stony Brook, NY) was used both for ECG, respiration, and temperature monitoring and for ECG triggering of the scans.

Magnetic resonance (MR) blood flow imaging was performed with the use of a two-dimensional (2D) spoiled gradient echo sequence with a bipolar gradient for the encoding of the 1D velocity normal to the slice. In this scheme, the phase of the reconstructed image maps the velocity, whereas the magnitude maps anatomical structure. Measurements were ECG triggered and taken every 5 ms during systole for a total of 50 ms, then every 10 ms during early diastole for an additional 50 ms, resulting in 16 time points per cardiac cycle. Because of gradient duty cycle limitations, each time point in the cardiac cycle was measured separately, so that the repetition time, TR, was the mouse cardiac cycle (typically 130–160 ms for anesthetized mice) and the echo time, TE, was 2 ms. An obliquely positioned, 2D localizer image showing the aorta plus at least two out of three of the innominate and left common carotid and left subclavian arteries was used to position a set of slices that cut through the ascending aorta and the carotid arteries just above the aortic arch. A slice thickness of 0.75 mm with a voxel size of 0.15 mm × 0.15 mm was used for the aortic slices, with two averaging steps for improved signal-to-noise ratio. Because of their smaller dimensions, a voxel size of 0.133 mm × 0.133 mm was used in the carotids with four averages. To minimize the number of slices necessary, a single, axially positioned slice was used for the innominate and left common carotid arteries. Although this prevented the slice from being exactly perpendicular to the artery axis, the flow rate calculation is essentially unaffected except for a minor change in partial volume error (41). More specifically, the decrease in velocity due to the nonperpendicular positioning should be compensated by the larger slice area of a nonperpendicular slice. All imaging was performed with a 7T MRI scanner (Inova; Varian, Palo Alto, CA).

Total blood volume crossing the imaging plane per cardiac cycle in each artery was obtained by first numerically integrating the velocities over the cross-sectional area of the artery and then integrating these values with respect to time. The artery cross section was manually segmented based primarily on the MR magnitude image. The segmentation was done separately for each time point to take into account vessel motion (Fig. 2).

Numerical simulation of blood flow. The geometry used for blood flow simulations was obtained by Batson's plastic casting of the aorta and major branches, followed by X-ray computerized tomography (CT) scanning of the casts (Fig. 3). Casts of the aorta and adjacent arteries were used to define aortic geometries. CD1 mice (Charles River) were heparinized with ~100 U/kg heparin intravenously via the tail vein. The left ventricle was cannulated at the apex with a 25-gauge angiocatheter, and the aorta was flushed with heparin saline to clear excess blood after major downstream branches of the aorta were tied off. A 4% paraformaldehyde solution in 0.1 mol/l phosphate buffer (pH 7.3) was perfused via the left ventricle at constant pressure (100 mmHg). The aorta was then injected at a controlled pressure (100–120 mmHg) with Batson's no. 17 Plastic Replica kit (Polysciences, Warrington, PA) using standard techniques (25). This pressure was held for 2–3 h while the plastic cured with the animal immersed in cold water and an ice bath to dissipate heat caused by

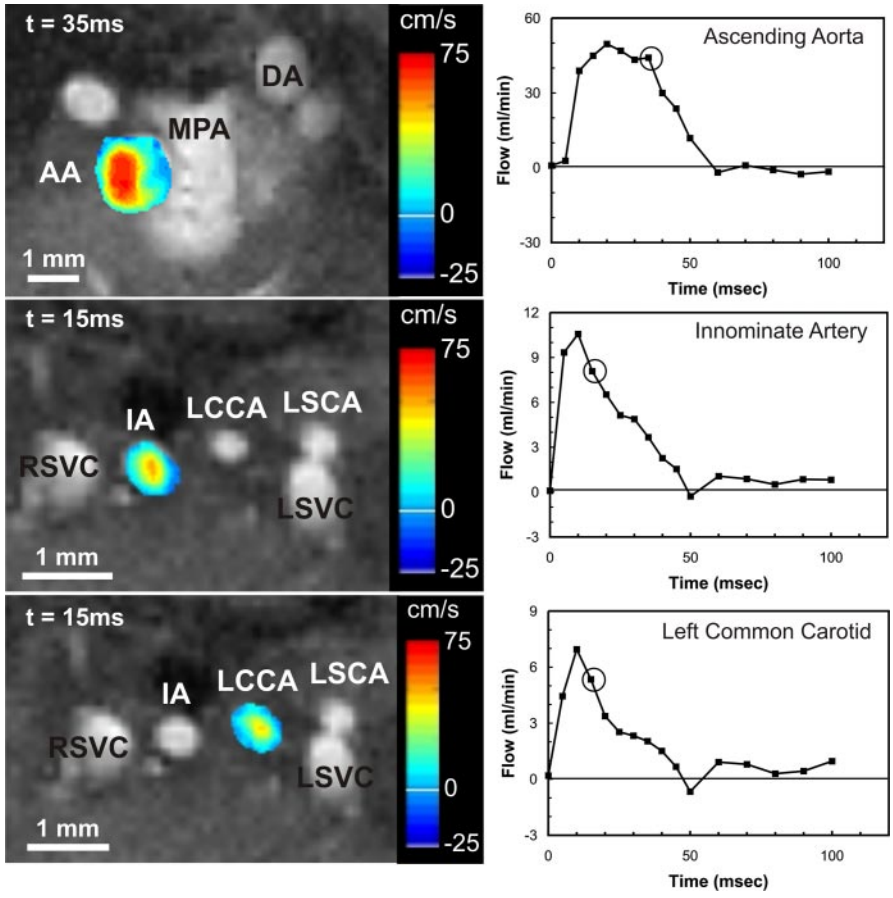

Fig. 2. High-resolution magnetic resonance (MR) imaging of blood flow patterns in the mouse aortic arch and its major branches taken from a single mouse. *Left*: two-dimensional (2D) MR magnitude images overlain with velocity data from a manually segmented region at a single time point in the cardiac cycle (marked by a circle on the time course plot shown at *right*). *Right*: corresponding time courses of the total flow in each vessel calculated by integration of the velocity in the segmented region, as described in the text. DA, descending aorta; MPA, main pulmonary artery; RSVC, right superior vena cava; LSVC, left superior vena cava.

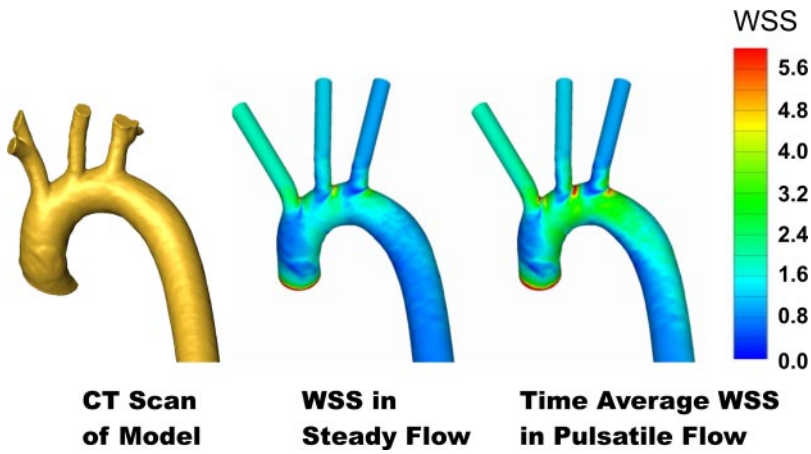

Fig. 3. Typical cast (*left*) and corresponding normalized wall shear stress (WSS) patterns computed under steady and unsteady flow conditions. The computerized tomography (CT) scan (shown here after segmentation in Amira) contains multiple branches, which are trimmed before addition of outlet extensions and surface smoothing to create a computational model. The WSS results show a close agreement between values computed in steady flow and the corresponding time-average values in unsteady flow. The normalizing value for WSS in this and all other figures is the shear stress that would exist in a long straight tube with diameter equal to aortic root diameter at the same mean flow rate and can be computed as $8\mu^2 \mathrm{Re}_D/(\rho D^2)$, where ρ and μ are blood density and viscosity, respectively. For a mouse aortic root diameter = 1.3 mm, this normalizing shear stress is 58 dynes/cm^2.

polymerization. After the cast had completely polymerized, the aorta was dissected free from the perivascular tissue and the cast was placed into a saturated KOH solution to remove adherent tissue. The resulting corrosion casts were cleaned in formic acid and distilled water and air dried.

Micro-CT scans of casts were performed with an MS-8 micro-CT imaging system (GE Medical Systems, London, ON, Canada) operating at 80 kV and 90 μA (28). Images were reconstructed using Microview software (GE Medical Systems) with a voxel size of 22 μm. The reconstructed images were segmented in Amira (Mercury Computer Systems, San Diego, CA) using an operator-defined threshold. Small vessels were trimmed to produce a model that included the ascending aorta, aortic arch, upper descending aorta, and the three major branch vessels emanating from the aortic arch. Extensions were added to the major branch vessels and the descending aorta using standard techniques (20) so as to ensure fully developed flow at the vessel outlets. A surface triangulation was generated and imported in ICEM-CFD (ICEM CFD Engineering, Berkeley, CA) and used to generate a tetrahedral finite element mesh, which was postprocessed by adding nodes to give P_2-P_1 Taylor-Hood finite elements. Preliminary studies showed that results were mesh independent in meshes containing 500,000–600,000 nodes, and all meshes adhered to this guideline.

The unsteady Navier-Stokes equations were numerically solved using a well-validated code (6) in four aortic arch models, and the resulting velocity fields were postprocessed to give wall shear stress fields. Newtonian blood rheology and stationary vessel walls were assumed. Steady flow simulations used either fully developed (parabolic) or plug (blunt) inlet boundary conditions at the aortic root. Unsteady flow simulations used either fully developed (Womersley profile) or a plug inlet velocity profile, both modulated in time as described below. On the basis of measurements (see RESULTS), the flow rates entering the innominate, left common carotid, and left subclavian arteries were specified to be 15%, 8%, and 7% of the blood flow rate entering the aortic root, respectively. Traction-free boundary conditions were imposed on the distal aortic outlet (7), and fully developed Dirichlet conditions were imposed at the outlets of major branch vessels.

A critical input into numerical simulations was the mean Reynolds number at the aortic root, defined as

$$\mathrm{Re}_D = \frac{VD}{\nu} = \frac{4\dot{Q}}{\pi D \nu} \qquad (1)$$

where V is the temporally and spatially averaged blood velocity at the aortic root, $\dot{Q}$ is the time-averaged cardiac output, D is vessel diameter (here taken as aortic root diameter), and ν is blood kinematic viscosity. Mouse blood viscosities were measured by rheometry and found to be very similar to those observed in humans (P. Ruengsakulrach, unpublished results). In particular, at the high shear rates appropriate for this study, an asymptotic effective kinematic viscosity of 3.5 cStokes is suitable. From the above equation, it can be seen that differences in Reynolds numbers between mice and humans will depend on the ratio of $\dot{Q}/D$.

In a preliminary study of nine CD1 mice, we found that aortic root diameter measured from casts, D (in mm), was linearly related to body mass, M (in g), by $D = 0.0284\,M + 0.08$ ($r^2 = 0.86$; body mass range 30–50 g). Using a cardiac output of 500 ml·min^{-1}·kg^{-1} measured in conscious instrumented mice of different body masses (16), we then computed the time-mean Reynolds number to be remarkably constant over a large range of mouse body masses, varying from 98 to 101 as body mass changes from 30 to 50 g. We therefore used a Reynolds number of 100 for all steady flow simulations. For unsteady flow simulations, the ascending aortic flow waveform measured by Janssen et al. (16) was scaled to have a mean Reynolds number of 100 and then used to specify aortic root volumetric blood flow rate as a function of time. On the basis of a resting heart rate of 600 beats/min and a typical aortic root diameter of 1 mm, the Womersley parameter was taken as 2.11 for unsteady simulations.

Virtual Doppler simulations. We used the computational fluid dynamics (CFD) data to generate "virtual" Doppler ultrasound spectra using a real-time and interactive Doppler ultrasound simulator (13, 21). Briefly, one CFD model (mouse CD3) was interrogated to identify the plane of the arch corresponding to that shown in the B-mode images. Sample volumes were then placed at inner and outer wall locations on that plane, roughly matching the locations and sizes of those in the corresponding B-mode images. Spectra were computed for each sample volume by matching the Doppler ultrasound parameters as closely as possible and displayed using approximately the same temporal and spatial resolutions. We also directly compared MRI-measured and computed velocity profiles at selected locations in the arch. For both Doppler and MRI comparisons, it was necessary to scale dimensionless computed velocities to actual velocities; to do so, we used a D = 1.3 mm and $\dot{Q}$ = 12 ml/min. These values were consistent with in vivo measurements in anesthetized mice (see RESULTS), and correspond to a mean Reynolds number of 56. This introduced a slight error, since our computed results were obtained at Reynolds number 100 (suitable for nonanesthetized conditions), but the error so introduced is likely less than experimental measurement error.

RESULTS

Representative Doppler velocity spectra for the ascending aorta, innominate, left common carotid, and left subclavian arteries are shown in Fig. 1. On the basis of temporal integration of the Doppler spectra averaged over three cardiac cycles

Table 1. *Results of ultrasound and MRI measurements in anesthetized mice*

Artery	Ultrasound		MRI	
	Blood Volume per Cardiac Cycle, μl	Flow Split, %	Blood Volume per Cardiac Cycle, μl	Flow Split, %
Ascending aorta	36.4±7.5	100	26.5±4.1	100
Innominate	5.5±1.4	15.3±1.5	4.5±0.8	16.9±1
Left common carotid	2.5±0.7	7.1±1.4	2.7±0.6	10.4±1.3
Left subclavian	2.2±0.2	6.4±1.4	ND	ND

Values are means ± SD for $n = 8$ mice. ND, not determined.

and averaged over eight mice, the flow rates and flow splits in these four arteries were computed (Table 1). Spatially skewed velocity profiles were evident in MR images in the aorta (Fig. 2), with higher-velocity blood traveling along the greater curvature, similar to the pattern seen in humans. Summation of instantaneous velocities over arterial cross sections yielded flow waveforms (Fig. 2), total flow rates, and flow splits (Table 1). Agreement on flow splits between Doppler ultrasound and MRI data was quite good, but there was a discrepancy in the total blood volume measured by these two techniques, although measured stroke volumes were within the range previously reported for anesthetized mice, e.g., (1, 15, 18). Because the ultrasound measurement uses a centrally placed sample volume to obtain a velocity, which is then multiplied by the vessel cross-sectional area to get flow, the Doppler data will tend to overestimate the total flow. This effect will be reduced as the sample volume size approaches the vessel diameter, so that the overestimation is expected to be less for smaller vessels. These trends are observed in Table 1, and we therefore regard the blood volume estimates from MRI as being slightly more accurate than those from ultrasound. The cardiac outputs from these measurements are of the order of 12 ml/min, slightly less than those measured in chronically instrumented conscious mice (16), which is consistent with the well-known fact that isoflurane anesthesia reduces cardiac output in mice (22, 37).

Computational modeling revealed complex flow patterns in the aorta that were consistent across all models. Although numerical simulations were carried out with a nonskewed velocity profile imposed at the aortic root, significant skewing was already evident just distal to the innominate artery (Fig. 4). The magnitude of this skewing was strongly dependent on Reynolds number. The form of these skewed velocity profiles was similar to that of Dean vortices, although the strength of the two vortices was very unequal. This led to asymmetric wall shear stresses, with largest wall shear stresses occurring on flow dividers to the major branch vessels, the greater curvature of the aortic arch, and the proximal side walls of the aortic arch. Smallest shear stresses were observed just proximal to major branch vessels and along the lesser curvature of the aortic arch.

We compared simulated and measured features of the velocity field in the aortic arch using Doppler ultrasonography and MRI velocimetry. Measured Doppler ultrasound velocity spectra showed clear qualitative differences between the greater curvature versus the lesser curvatures of the arch, as expected from the skewed nature of the velocity patterns in the arch (Fig. 5). The simulated Doppler spectra at these locations reproduced the main features of the measured spectra quite well, including the pronounced spectral broadening and end-systolic retrograde flow present along the lesser curvature but absent on the greater curvature. Velocity profiles measured by using MRI also show flow asymmetries across the artery (Fig. 6). The computational modeling slightly underpredicted the skewing of the velocity profile toward the greater curvature, particularly at peak systole. Overall, however, the qualitative correspondence was reasonable and indicated that the computational modeling was capturing the main features of the flow. Quantitatively, simulated spectra and computed velocity distributions differed slightly from the measured values, an effect that will be further discussed in DISCUSSION.

Comparison between simulated and measured velocities showed reasonable qualitative agreement (Figs. 5 and 6), enhancing confidence in the simulation results. Nonetheless, there was some discrepancy between simulated and measured velocities. In the case of the Doppler ultrasound comparison (Fig. 5), the simulated velocities were somewhat less than the measured values, an effect that can readily be explained by uncertainties about the actual vessel diameter, flow rate, and sample volume placement. In the case of the MR measurements, the discrepancy was in the opposite direction. This may be due to limitations in temporal and spatial resolution in the MR measurements, leading to experimental underestimation of velocities, particularly near the systolic flow peak (41), as well as uncertainty about the actual vessel diameter.

Because of uncertainties in experimental measurements, it is prudent to enquire how sensitive our results are to changes in input parameters, such as aortic root velocity profile, the flow splits into major branch vessels, and the shape of the cardiac output waveform. Changing the velocity profile at the aortic root (blunted vs. fully developed) qualitatively altered the velocity and wall shear stress patterns, but changes in wall shear stress patterns were only notable in the proximal aorta, with little change evident in the arch and descending aorta. This indicates that blood flow patterns in and distal to the arch are determined primarily by the geometry of the vessel. Altering the flow splits imposed on the major branch vessels within reasonable physiologic limits produced modest quantitative changes in the WSS distributions but no qualitative differences. Finally, comparison of WSS distributions for steady flow versus time-averaged values in pulsatile flow showed only modest effects (Fig. 3), with a slight increase in WSS values on the side walls and in small islands at the major branch vessel flow dividers. These effects are explainable in terms of stronger secondary flows occurring near peak systole in the pulsatile case. Considering how similar the steady and unsteady results appear, we expect little effect due to changing flow waveform, at least on time-averaged WSS profiles.

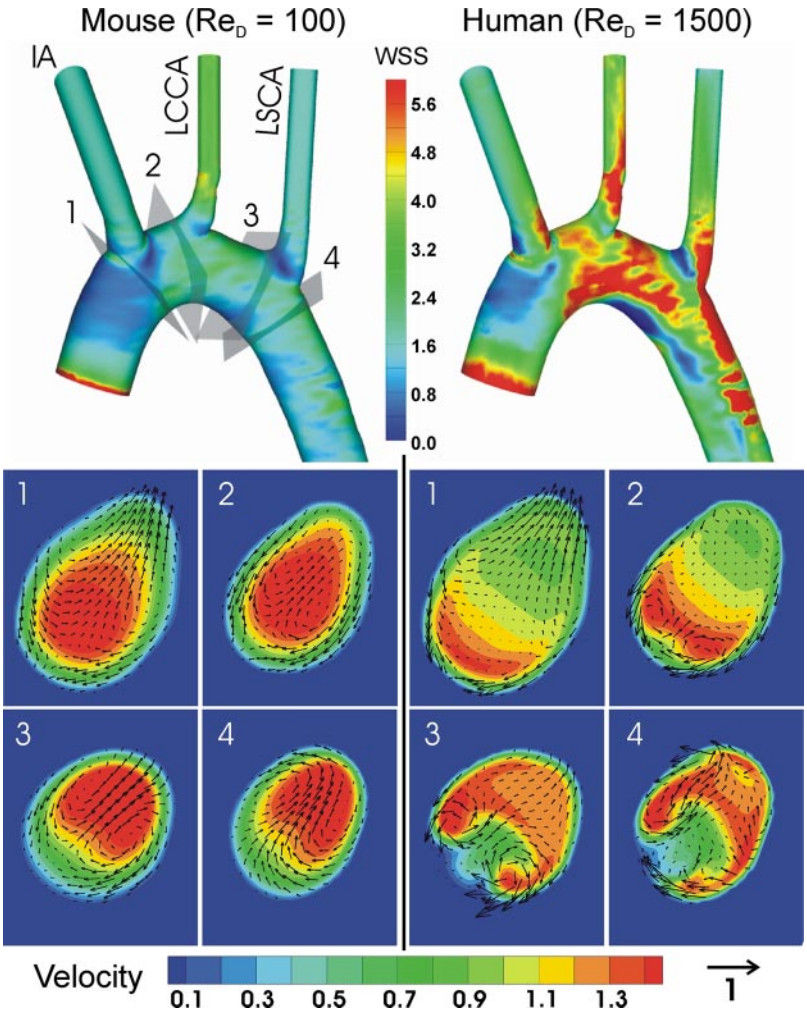

Fig. 4. Comparison of normalized wall shear stresses (*top*) and normalized velocities on selected cross-sectional slices (*bottom*) for steady flow in a single aortic model at Reynolds numbers (Re_D; see *Eq. 1*) typical of mouse (*left*) and human (*right*) aortic root diameters. Cross-sectional slices show through-plane velocities (color) and in-plane velocities (arrows) at cross sections identified by numbers 1–4 in *top left* panel. Shear stress normalization follows the same convention as in Fig. 3: for mice, normalizing shear stress = 58 dynes/cm^2 for a 1.3-mm diameter aortic root, whereas for humans, the normalizing shear stress = 1.63 dynes/cm^2 for a 30-mm diameter aortic root (40). Velocities are normalized by the mean inlet velocity, which for the mouse is 26.9 cm/s and for the human is 17.5 cm/s. Slices on which velocities are extracted are oriented so that the inner and outer curvatures are at the bottom left and top right corners of each panel, respectively.

Our data show important differences between the hemodynamic environment in the mouse and human aortic arches. First, the mean level of WSS in the mouse is much larger than in the human (~60 dynes/cm^2 vs. ~2 dynes/cm^2), consistent with previous studies (10, 24). Second, blood flow simulations at Reynolds numbers typical of humans (~1,500) show a much larger asymmetry in the wall shear stress environment between the greater and lesser curvatures when compared with simulations at typical mouse Reynolds numbers (Fig. 4). This difference is entirely explainable by the much stronger secondary

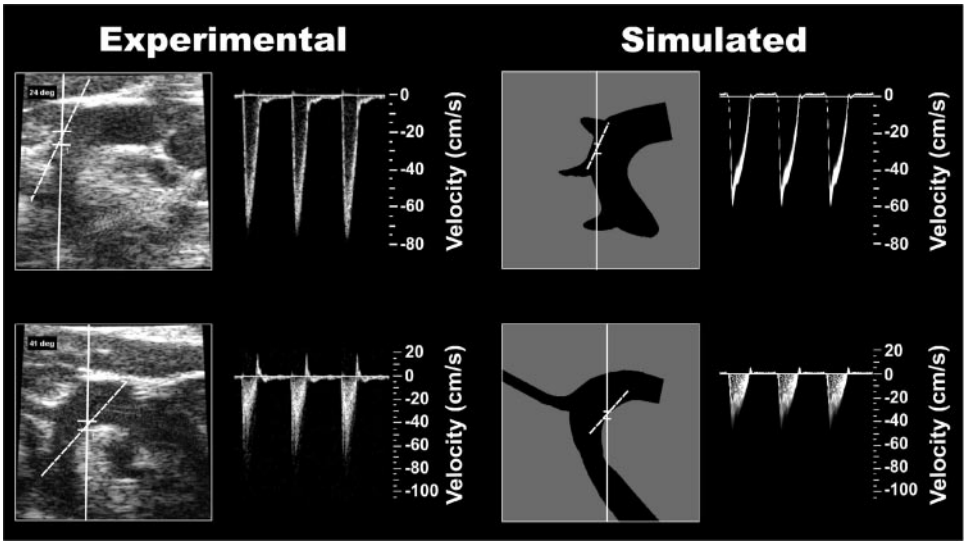

Fig. 5. Comparison of experimentally measured vs. simulated Doppler spectra for sample volumes placed at corresponding locations near the greater curvature (*top*) and lesser curvature (*bottom*) of the aortic arch. Qualitatively, there is good agreement between the measured and simulated spectra, with a slight underestimation of retrograde flow along the lesser curvature in the simulated spectra. Solid lines in the B-mode anatomical images represent beam axes, with sample volume contained between the two perpendicular line segments. The operator-defined local vessel axis is shown by the dashed lines. The aortic root is at the top right of the B-mode anatomical images. The simulated spectra were generated by assuming an aortic root diameter of D = 1.3 mm and a cardiac output of $\dot{Q}$ = 12 ml/min, appropriate for the anesthetized 25-g C57BL/6 mice used for MR imaging.

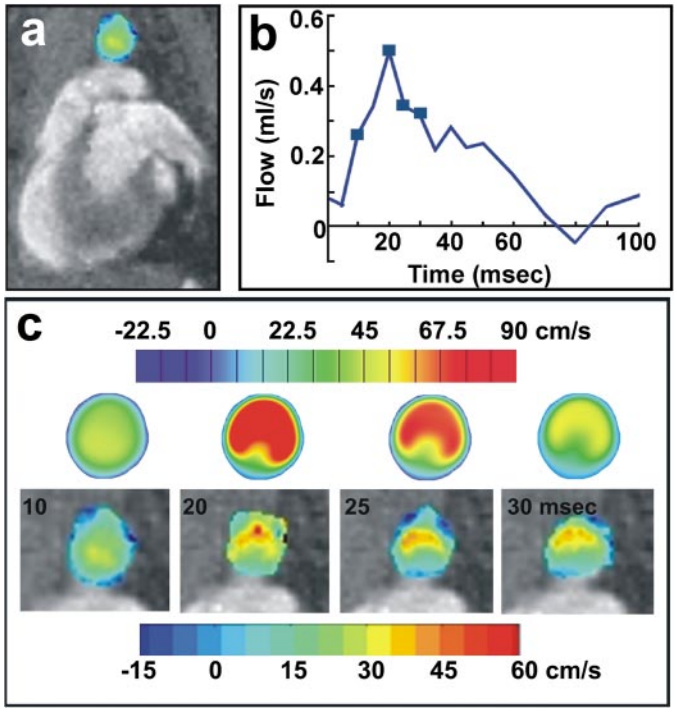

Fig. 6. Comparison of velocity profiles measured with MRI vs. computed velocity profiles. *a*: anatomical image showing heart in sagittal plane, with through-plane velocities in the aortic arch shown in color above the heart. *b*: measured instantaneous flow rates at the measurement plane shown in *a*. Squares indicate instants at which comparison between experiment and simulation is shown in *c*. *c*: numerically computed (*top*) and experimentally measured (*bottom*) through-plane velocities in the aortic arch near slice *plane 3* of Fig. 4. The MR images correspond to the colored region in *a* at the indicated times. The simulated velocities correspond to an aortic root diameter of $D = 1.3$ mm and a cardiac output of $\dot{Q} = 12$ ml/min, appropriate for the anesthetized 25-g C57BL/6 mice used for MRI.

flows present in the human, driven by the human's higher mean Reynolds number. In fact, when average wall shear stresses along the inner and outer walls are plotted versus Reynolds number, it can be seen that the inner-outer wall stresses begin to diverge at Reynolds numbers typical of animals just slightly larger than the mouse (Fig. 7).

DISCUSSION

Our findings demonstrate that the hemodynamic environment in the mouse aortic arch differs in important ways from the environment in the human. Specifically, the human shows greater spatial variability in normalized wall shear stress than does the mouse, i.e., in humans, the lows are relatively lower and the highs are relatively higher when compared with the mouse. This result is initially surprising, considering the anatomical similarity of the aortic arch in the two species, as well as the similarity in such important physiological variables as blood pressure and blood velocity. However, these interspecies differences can be understood in terms of physical scaling arising from the Navier-Stokes equations. In particular, the Reynolds number, which is proportional to the ratio of inertial to viscous forces and hence drives much of the interesting hemodynamic features, is much smaller in the mouse, creating less secondary flows and a more uniform hemodynamic environment. In fact, the in vivo situation in the mouse may be even more homogeneous than we predict here: the mouse Reynolds number used in this study was based on aortic root diameters measured from casts. Casting can underestimate in vivo vessel diameters (30), and, in fact, both our MRI and ultrasound measurements on 25-g C57BL/6 mice in the ascending aorta ~1 mm above the root suggest a diameter of 1.3 mm, consistent with previous measurements (11). *Equation 1* demonstrates that an increase in diameter, for a given flow rate $\dot{Q}$, will produce a lower Reynolds number. We therefore view our time-averaged Reynolds number of 100, which was based on cast dimensions, as an upper bound, and suggest that the results presented here may overestimate spatial heterogeneity in the mouse.

The reduced heterogeneity seen in the mouse is biologically interesting because it is precisely this hemodynamic heterogeneity that has been used to explain the propensity for atherosclerotic lesions to form at certain locations in the arterial tree (34). Our results suggest that a more uniform distribution of lesions might be expected in the mouse aortic arch as compared with the human situation. However, experimental evidence contradicts this expectation: lesions are relatively absent in the aortic arch in humans [except near major branch ostia (5)] yet

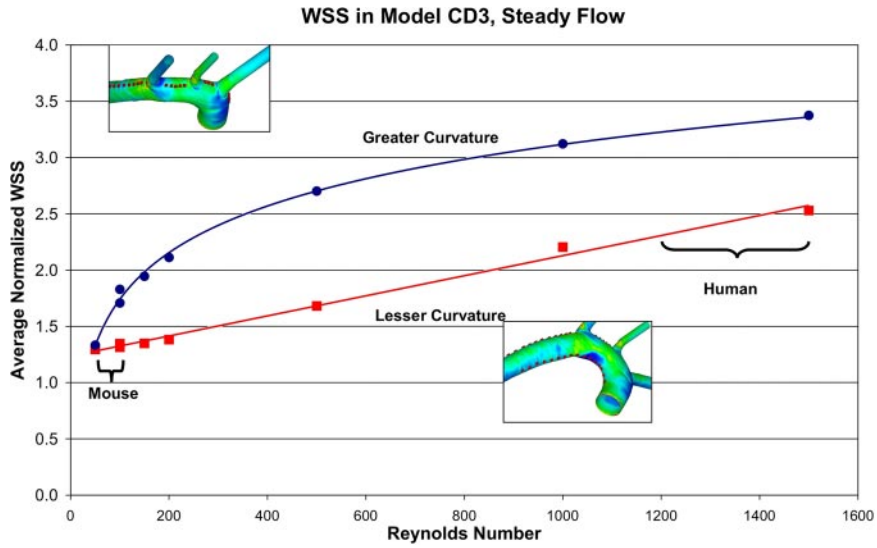

Fig. 7. Plot of average normalized wall shear stress on the greater and lesser curvatures in the aortic arch under steady flow conditions as a function of Reynolds number an a single model. A single value for WSS along each of the greater and lesser curvatures was obtained by extracting WSS values at discrete points (shown by red dots) and averaging the point values. Extraction points were chosen to avoid the inlet region and extreme values of WSS associated with the flow dividers of the major branch vessels. Shear stress normalization follows the same convention as in Figs. 3 and 4.

show a high propensity for the lesser curvature in the mouse aortic arch (27, 32, 39), consistent with colocalization of other proatherogenic markers such as lipid hyperpermeability (27), VCAM-1 recruitment (33), and NF-κB activation (12) in the mouse. Considering the actual magnitude of shear stresses in mice versus humans, it is particularly interesting that the lesser curvature of the human arch is a region of low and oscillating shear stress, whereas the lesser curvature of the mouse arch is exposed to a much higher time-averaged shear stress. Since low and oscillating shear stress is usually considered to be proatherogenic (23), it might be expected that the lesser curvature of the human arch region would show a greater propensity for lesions than are observed in the mouse. How can one explain this apparent "decoupling" between the hemodynamic environment and lesion propensity in the mouse? One possibility is that factors other than wall shear stress alone are important in localizing lesion patterns. Another possibility is that the mouse endothelium responds to shear stress in a different manner than does human endothelium. For example, we have expressed all shear stresses as values normalized by a species-specific typical value (here taken as the shear stress at the aortic root for fully developed flow), reasoning that variations away from this baseline value would be biologically significant. In other words, considering the physiological variations in shear stress due to exercise, changes of posture, etc., we assume that if a vascular endothelial cell in a mouse is typically exposed to a shear stress of 60 dynes/cm^2, a 5 dynes/cm^2 change would have a smaller biological effect than in a human, where the "baseline" shear stress is only several dynes/cm^2. This assumption may not be correct. No matter what the explanation, it surely seems interesting to further investigate the relationship between hemodynamics and lesion formation in the mouse.

It is of interest to ask how errors in the experimental inputs propagated to errors in the computed wall shear stresses. There were two main sources of experimental error: uncertainty about the vessel dimensions in the casts and uncertainty about flow rates estimated from MRI and ultrasound. The micro-CT system used to scan the casts had a spatial resolution of 22 μm, so we can estimate the error in geometric shape of the vessels to be ~40–45 μm, which is 3–4% of aortic root diameter. Since shear stress scales as the inverse cube of vessel diameter, this implies a wall shear stress error of order 10–15%. For the MR imaging of blood velocity, the signal-to-noise ratio was ~50, resulting in a phase noise and hence a velocity error of ±5 cm/s per voxel, or ~5% of the systolic blood velocity in the aorta. When this is integrated over all voxels covering the vessel and over all the time points in the cardiac cycle, the error is much lower and is much less than the mouse-to-mouse physiological variability (see, e.g., standard deviations in blood volumes of about ±20–25% reported in Table 1). For the Doppler ultrasound measurements, which can be made over a single heart beat, the variability in the flow from one heartbeat to the next can be seen directly and exceeds the error associated with measuring flow in a single heartbeat. Again, the accuracy in the ultrasound measurement for individual mice is considerably better than the biological variability from one mouse to the next. Errors in shear stress are linearly proportional to errors in flow rate and are therefore expected to be less than the inter-mouse variability of ±20–25%. These errors are much smaller than the difference in shear between mice and humans and also much less than the dynamic range of shear stresses in the mouse aorta. Considering the approximations made in the modeling (see next paragraph), we therefore believe that experimental errors will not materially affect the conclusions of this work.

It is important to point out the limitations of this work. All experimental measurements in the mouse are challenging because of the small caliber of vessels, and therefore there is uncertainty in the experimental input values to the numerical modeling. However, our sensitivity analysis suggested that our conclusions were robust to such uncertainty. Our numerical modeling did not incorporate non-Newtonian blood rheology and aortic motion. Non-Newtonian rheology is expected to be unimportant at the high shear rates typical of the mouse arterial system. Aortic motion may be a more significant effect: previous studies have shown that it influences aortic hemodynamics (19, 31). Another potentially important factor is the shape of the velocity profile specified in numerical modeling at the aortic root. Experimental measurements show that this is skewed toward the greater curvature and that the extent of skewing varies throughout the cardiac cycle. We did not incorporate this effect, which likely explains some of the discrepancies between computed and measured velocities. Future modeling work should consider aortic motion effects and aortic root velocity profile skewing, although we expect that arguments about Reynolds number scaling will be largely unaffected by these effects.

Finally, we have focused here on the aortic arch because it is feasible to make experimental measurements at this location. However, there is nothing unique about the arch; we would expect similar interspecies differences in Reynolds number to drive differences in the hemodynamic environment at other locations of curvature and bifurcation as well.

ACKNOWLEDGMENTS

The authors thank Samira Hirji for assistance with the Doppler ultrasound simulations and Jaques Milner for assistance with flow simulations and data processing.

GRANTS

This study was supported by the Natural Sciences and Engineering Research Council (to C. R. Ethier and D. A. Steinman), the Canada Foundation for Innovation (to R. M. Henkelman), The Royal Golden Jubilee Ph.D. Program, Thailand Research Fund (to P. Ruengsakulrach), and a Career Investigator Award from the Heart & Stroke Foundation of Ontario (to D. A. Steinman).

DISCLOSURE

F. S. Foster holds a financial interest in VisualSonics.

REFERENCES

1. **Constantinesco A, Choquet P, Monassier L, Israel-Jost V, Mertz L.** Assessment of left ventricular perfusion, volumes, and motion in mice using pinhole gated SPECT. *J Nucl Med* 46: 1005–1011, 2005.
2. **Daugherty A.** Mouse models of atherosclerosis. *Am J Med Sci* 323: 3–10, 2002.
3. **Davies PF.** Spatial hemodynamics, the endothelium, and focal atherogenesis: a cell cycle link? *Circ Res* 86: 114–116, 2000.
4. **Dazai J, Bock NA, Nieman BJ, Davidson LM, Henkelman RM, Chen XJ.** Multiple mouse biological loading and monitoring system for MRI. *Magn Reson Med* 52: 709–715, 2004.
5. **DeBakey ME, Lawrie GM, Glaeser DH.** Patterns of atherosclerosis and their surgical significance. *Ann Surg* 201: 115–131, 1985.

6. **Ethier CR, Prakash S, Steinman DA, Leask RL, Couch GG, Ojha M.** Steady flow separation patterns in a 45 degree junction. *J Fluid Mech* 411: 1–38, 2000.
7. **Ethier CR, Steinman DA, Ojha M.** Comparisons between computational hemodynamics, photochromic dye flow visualization and MR velocimetry. In: *The Haemodynamics of Internal Organs—Comparison of Computational Predictions With In Vivo and In Vitro Data*, edited by Xu XY and Collins MW. Ashurst, UK: Computational Mechanics, 1999, p. 131–184.
8. **Friedman MH.** Arteriosclerosis research using vascular flow models: from 2-D branches to compliant replicas. *J Biomech Eng* 115: 595–601, 1993.
9. **Getz GS, Reardon CA.** Diet and murine atherosclerosis. *Arterioscler Thromb Vasc Biol* 26: 242–249, 2006.
10. **Greve JM, Les AS, Tang BT, Draney Blomme MT, Wilson NM, Dalman RL, Pelc NJ, Taylor CA.** Allometric scaling of wall shear stress from mice to humans: quantification using cine phase-contrast MRI and computational fluid dynamics. *Am J Physiol Heart Circ* Physiol 291: H1700–H1708, 2006.
11. **Guo X, Kono Y, Mattrey R, Kassab GS.** Morphometry and strain distribution of the C57BL/6 mouse aorta. *Am J Physiol Heart Circ Physiol* 283: H1829–H1837, 2002.
12. **Hajra L, Evans AI, Chen M, Hyduk SJ, Collins T, Cybulsky MI.** The NF-kappa B signal transduction pathway in aortic endothelial cells is primed for activation in regions predisposed to atherosclerotic lesion formation. *Proc Natl Acad Sci USA* 97: 9052–9057, 2000.
13. **Hirji S, Downey DB, Holdsworth DW, Steinman DA.** Real-time and interactive virtual Doppler ultrasound. In: *Medical Imaging 2005*: *Ultrasonic Imaging and Signal Processing. Proceedings of the SPIE-International Society for Optical Engineering*, edited by Walker WF and Emelianov SY. Bellingham, WA: SPIE, 2005, vol. 5750, p. 127–138.
14. **Iiyama K, Hajra L, Iiyama M, Li H, DiChiara M, Medoff BD, Cybulsky MI.** Patterns of vascular cell adhesion molecule-1 and intercellular adhesion molecule-1 expression in rabbit and mouse atherosclerotic lesions and at sites predisposed to lesion formation. *Circ Res* 85: 199–207, 1999.
15. **Jacoby C, Molojavyi A, Flogel U, Merx MW, Ding Z, Schrader J.** Direct comparison of magnetic resonance imaging and conductance microcatheter in the evaluation of left ventricular function in mice. *Basic Res Cardiol* 101: 87–95, 2006.
16. **Janssen B, Debets J, Leenders P, Smits J.** Chronic measurement of cardiac output in conscious mice. *Am J Physiol Regul Integr Comp Physiol* 282: R928–R935, 2002.
17. **Janssen BJ, De CT, Debets JJ, Brouns AE, Callahan MF, Smith TL.** Effects of anesthetics on systemic hemodynamics in mice. *Am J Physiol Heart Circ Physiol* 287: H1618–H1624, 2004.
18. **Janssen BJ, Smits JF.** Autonomic control of blood pressure in mice: basic physiology and effects of genetic modification. *Am J Physiol Regul Integr Comp Physiol* 282: R1545–R1564, 2002.
19. **Jin S, Oshinski J, Giddens DP.** Effects of wall motion and compliance on flow patterns in the ascending aorta. *J Biomech Eng* 125: 347–354, 2003.
20. **Joshi AK, Leask RL, Myers JG, Ojha M, Butany J, Ethier CR.** Intimal thickness is not associated with wall shear stress patterns in the human right coronary artery. *Arterioscler Thromb Vasc Biol* 24: 2408–2413, 2004.
21. **Khoshniat M, Thorne ML, Poepping TL, Hirji S, Holdsworth DW, Steinman DA.** Real-time numerical simulation of Doppler ultrasound in the presence of nonaxial flow. *Ultrasound Med Biol* 31: 519–528, 2005.
22. **Kober F, Iltis I, Cozzone PJ, Bernard M.** Cine-MRI assessment of cardiac function in mice anesthetized with ketamine/xylazine and isoflurane. *MAGMA* 17: 157–161, 2004.
23. **Ku DN, Giddens DP, Zarins CK, Glagov S.** Pulsatile flow and atherosclerosis in the human carotid bifurcation: positive correlation between plaque location and low and oscillating shear stress. *Arteriosclerosis* 5: 293–302, 1985.
24. **Langille BL.** Remodeling of developing and mature arteries: endothelium, smooth muscle, and matrix. *J Cardiovasc Pharmacol* 21, *Suppl* 1: S11–S17, 1993.
25. **Leask RL, Butany J, Johnston KW, Ethier CR, Ojha M.** Human saphenous vein coronary artery bypass graft morphology, geometry and hemodynamics. *Ann Biomed Eng* 33: 301–309, 2005.
26. **Lee K, Forudi F, Saidel GM, Penn MS.** Alterations in internal elastic lamina permeability as a function of age and anatomical site precede lesion development in apolipoprotein E-null mice. *Circ Res* 97: 450–456, 2005.
27. **Lichtman AH, Clinton SK, Iiyama K, Connelly PW, Libby P, Cybulsky MI.** Hyperlipidemia and atherosclerotic lesion development in LDL receptor-deficient mice fed defined semipurified diets with and without cholate. *Arterioscler Thromb Vasc Biol* 19: 1938–1944, 1999.
28. **Marxen M, Thornton MM, Chiarot CB, Klement G, Koprivnikar J, Sled JG, Henkelman RM.** MicroCT scanner performance and considerations for vascular specimen imaging. *Med Phys* 31: 305–313, 2004.
29. **Meir KS, Leitersdorf E.** Atherosclerosis in the apolipoprotein-E-deficient mouse: a decade of progress. *Arterioscler Thromb Vasc Biol* 24: 1006–1014, 2004.
30. **Moore JA, Rutt BK, Karlik SJ, Yin K, Ethier CR.** Computational blood flow modeling based on in vivo measurements. *Ann Biomed Eng* 27: 627–640, 1999.
31. **Mori D, Yamaguchi T.** Computational fluid dynamics modeling and analysis of the effect of 3-D distortion of the human aortic arch. *Comput Methods Biomech Biomed Engin* 5: 249–260, 2002.
32. **Nakashima Y, Plump AS, Raines EW, Breslow JL, Ross R.** ApoE-deficient mice develop lesions of all phases of atherosclerosis throughout the arterial tree. *Arterioscler Thromb* 14: 133–140, 1994.
33. **Nakashima Y, Raines EW, Plump AS, Breslow JL, Ross R.** Upregulation of VCAM-1 and ICAM-1 at atherosclerosis-prone sites on the endothelium in the ApoE-deficient mouse. *Arterioscler Thromb Vasc Biol* 18: 842–851, 1998.
34. **Nerem RM.** Atherogenesis: hemodynamics, vascular geometry, and the endothelium. *Biorheology* 21: 565–569, 1984.
35. **Ohashi R, Mu H, Yao Q, Chen C.** Cellular and molecular mechanisms of atherosclerosis with mouse models. *Trends Cardiovasc Med* 14: 187–190, 2004.
36. **Quinones MA, Otto CM, Stoddard M, Waggoner A, Zoghbi WA.** Recommendations for quantification of Doppler echocardiography: a report from the Doppler Quantification Task Force of the Nomenclature and Standards Committee of the American Society of Echocardiography. *J Am Soc Echocardiogr* 15: 167–184, 2002.
37. **Roth DM, Swaney JS, Dalton ND, Gilpin EA, Ross J Jr.** Impact of anesthesia on cardiac function during echocardiography in mice. *Am J Physiol Heart Circ Physiol* 282: H2134–H2140, 2002.
38. **Sahn DJ, DeMaria A, Kisslo J, Weyman A.** Recommendations regarding quantitation in M-mode echocardiography: results of a survey of echocardiographic measurements. *Circulation* 58: 1072–1083, 1978.
39. **VanderLaan PA, Reardon CA, Getz GS.** Site specificity of atherosclerosis: site-selective responses to atherosclerotic modulators. *Arterioscler Thromb Vasc Biol* 24: 12–22, 2004.
40. **Vasan RS, Larson MG, Levy D.** Determinants of echocardiographic aortic root size. The Framingham Heart Study. *Circulation* 91: 734–740, 1995.
41. **Wolf RL, Ehman RL, Riederer SJ, Rossman PJ.** Analysis of systematic and random error in MR volumetric flow measurements. *Magn Reson Med* 30: 82–91, 1993.
42. **Wong AY, Kulandavelu S, Whiteley KJ, Qu D, Langille BL, Adamson SL.** Maternal cardiovascular changes during pregnancy and postpartum in mice. *Am J Physiol Heart Circ Physiol* 282: H918–H925, 2002.
43. **Zarins CK, Zatina MA, Giddens DP, Ku DN, Glagov S.** Shear stress regulation of artery lumen diameter in experimental atherogenesis. *J Vasc Surg* 5: 413–420, 1987.
44. **Zhou YQ, Foster FS, Nieman BJ, Davidson L, Chen XJ, Henkelman RM.** Comprehensive transthoracic cardiac imaging in mice using ultrasound biomicroscopy with anatomical confirmation by magnetic resonance imaging. *Physiol Genomics* 18: 232–244, 2004.